Onboard Autonomous Rock Shape Analysis For Mars Rovers *

Justin Fox †
jfox@its.caltech.edu

Rebecca Castaño‡
Rebecca.Castano@jpl.nasa.gov

Robert C. Anderson‡
robert.c.anderson@jpl.nasa.gov

†California Institute of Technology
Pasadena, CA 91125

‡ Jet Propulsion Laboratory (JPL)
California Institute of Technology
Pasadena, CA 91109

Abstract – In the quest to maximize the scientific return of future robotic missions, it is imperative that our rovers be capable of determining the importance of the science they collect so that they may prioritize the acquisition and relay of that data. As an important step in this process, we present an automated technique to allow a rover to classify the shape and other geologic characteristics of rocks from two-dimensional photographic images and three-dimensional stereographically produced data. Experiments were conducted in the Matlab environment using images returned by JPL's Mars Pathfinder mission.

Our method begins by first segmenting the rocks from the background using a combination of image intensity and height data. Various metrics are then used to classify the region's sphericity, roundness, and other geometric properties. Preliminary experiments to determine the most useful metrics were conducted by characterizing the two-dimensional rock shape while the three-dimensional shape was later studied with metrics derived from these two-dimensional techniques.

Seven measures were developed and implemented. The performance of each measure was characterized by analyzing images from the Pathfinder mission and ranking the rocks according to the measured properties. Combined, the measures would provide a tool by which an automated rover could discover a greater amount of information about the data it collects, leading to a more productive mission.

TABLE OF CONTENTS

1. INTRODUCTION

Since it may be a long time before manned missions to other planets or planetary bodies become a reality, it is necessary to design the robotic explorers we do send to be astute and meticulous observers with the ability to mimic the work of human geologists and scientists as nearly as possible. Rovers must be able to understand the purpose behind their exploration, to determine how best to accomplish that purpose, and, most basic of all, to make judgements about the world they view and to categorize that world in ways which will help them to achieve their goals. To this end, a rover must become a 'robotic geologist,' not merely seeing rocks and surface features, but understanding, characterizing, and studying them.

One important and geologically useful feature of rocks is their inherent shape. The shape of a rock is a complex property which is oftentimes difficult to describe precisely. However, a great deal of geological work has been performed classifying and categorizing the general appearance of microscopic particle grains with respect to various concrete properties [1], [6], [9], [13] [18], and the same basic concepts remain applicable even when scaled to the macroscopic realm of Martian rocks. In particular, the concepts of roundness and sphericity provide indicative measures of a rock's shape which might be used by a rover to obtain valuable information about the specimen's geologic origins and history [3], [15].

Roundness is a measure which indicates the sharpness of an object's corners and the angularity of its edges. The accepted quantifiable definition of this property, attributed to Wadell (1932), involves finding the ratio of the average radius of curvature of the corners to the radius of the largest inscribed circle. In the past, if this measure was desired there were two possible methods of acquiring it. One method was to have a person compare a particle to images of particles with known roundness, and in this way determine on a relative scale the specimen's roundness. The other method required a two-dimensional photograph of a rock to be taken and then enlarged to some standard size. Then the average radius of curvature was painstakingly calculated by hand, or, due to the difficulty of this calculation, the radius of curvature at merely the most angular corner would be found. Next, special premeasured circles would be manually fit to the rock grain un-

*IEEEAC paper #276
0-7803-7231-X/01/$10.00/

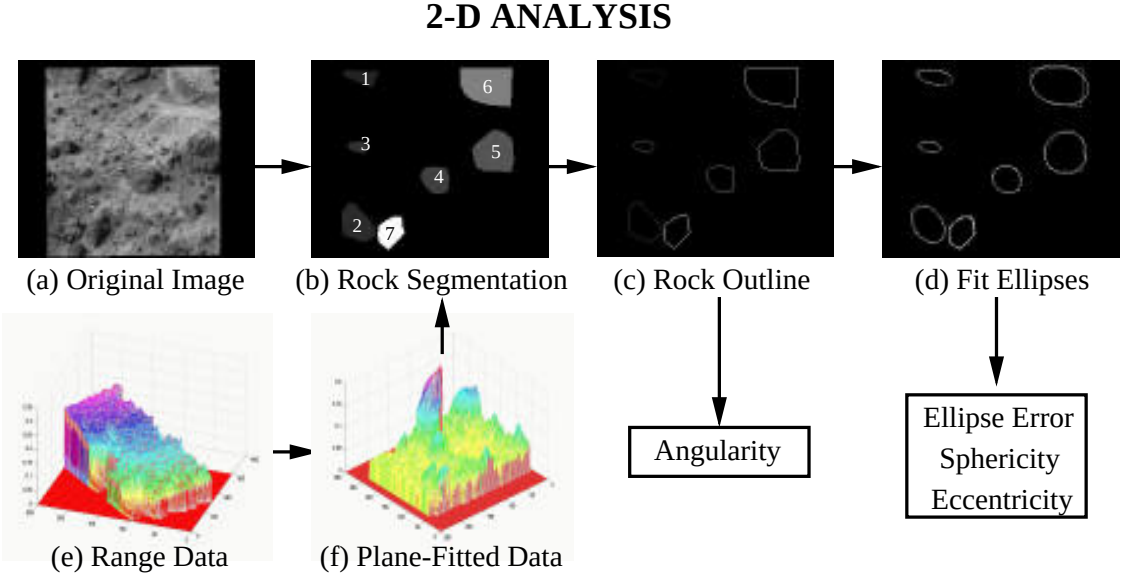

Figure 1: A flow chart of the two-dimensional analysis of an image $(\mathbf{a})$. The process begins with the segmentation of the rocks from the image background $(\mathbf{b})$ using the plane-fitted range data $(\mathbf{f})$. Outlines of the rocks are then found via edge detection $(\mathbf{c})$. These outlines are next used to calculate the two-dimensional angularity of the rocks through the modified corner-finding algorithm described below. Ellipses are also fit to the outlines $(\mathbf{d})$ by an analytic least-squares fitting method. Finally, the sphericity, eccentricity, and ellipse-fitting error can be calculated from the fit ellipses. The entire process requires less than 2 minutes per image running in unoptimized Matlab code on a Sun Ultra 60.

til the maximum inscribed circle was found [15]. Obviously this process was time-consuming and laborious. However, we present instead an automatic method of calculating an estimate of the relative roundness of a rock which involves the calculation of the average maximum peak angle of certain inscribed triangles. Not only is this method automated, but it can also conceivably obtain a precision which human estimation and categorization hitherto could not.

Sphericity refers to larger scale shape characteristics than roundness. Sphericity identifies how well a particle or rock approaches a truly spherical shape. It was again Wadell who defined a measure for sphericity. Wadell's sphericitiy involved the assumption that the rock was a regular triaxial ellipsoid and the calculation of the three perpendicular axes of that ellipsoid, dL, dI, and dS, being the longest, intermediate, and shortest dimensions, respectively. The Wadell sphericity was then defined as:

$$\psi_W = \sqrt[3]{\frac{d_S d_I}{d_L^2}} \tag{1}$$

Sneed and Folk (1958) modified Wadell's definition, developing what is known as the maximum projection sphericity which we use here

$$\psi_P = \sqrt[3]{\frac{d_S^2}{d_L d_I}} \tag{2}$$

It is this measure that we will hereafter refer to simply as sphericity.

It was our objective to conceive the methods by which an automated rover could calculate both the roundness and the sphericity of the rocks in an image using only the two-dimensional images and stereographic range data. With these characteristics, it would be possible for the rover to estimate important information, such as how far the rock had travelled from its source, the direction of the fluid flow, and whether the rock was of the same general age as those surrounding it. We hoped by this process to grant the rover a better understanding of the region it studied and in that way increase the scientific return of the mission.

2. METHODS

Rock Segmentation

Our first task was to use the three-dimensional stereographic range data to segment the rocks in the image from the background. We used the method described in [11] which we briefly overview here. The range data that we used contained the x, y, and z coordinates of every pixel in the image based on an arbitrary camera-based coordinate system. In order to obtain the actual height of the rocks above the ground, it was necessary to use a least squares plane-fitting method such as the one described in [14]. The plane was initially fit to every point in the image, and successive iterations were then performed by rejecting those points whose distance from

the plane was greater than three standard deviations from the mean. In this way, the plane was fit as closely as possible to the points nearest to the mean height in the image, which we assumed to be a good indication of ground height. Having obtained this more or less topographical map of the image, the tops of rocks were next identified, being those regions whose neighbors were all lower than the prospective top. Those regions whose neighbors were both above and below them were labelled as the sides of rocks, and, of course, minimums were labelled as bottoms. The rocks were in this way reconstructed from the three-dimensional stereographic data with the tops being combined with sides until a bottom region was encountered. For more information on this segmentation technique, please see [11].

Two-Dimensional Shape Characterization

We began by first characterizing the two-dimensional shapes of the rocks and later modified or revised our methods for three-dimensions as appropriate. The general procedure we developed for two-dimensional analysis (Figure 1) was to first obtain an outline of each segmented rock from the output of the rock segmentation module described above using simple edge-finding techniques. Next, the least-squares best-fitting ellipse was calculated for the data points on the outline of the rock, and the ellipse-fitting error as well as the eccentricity of the fit ellipse was reported. Finally, we applied a modified corner-finding algorithm to determine the angularity or roundness of the rock. The results were then recorded for comparison and spot-checked for accuracy by expert geologists.

Ellipse Fitting – The ellipse fitting was performed by Matlab code originally produced by Fitzgibbon, Pilu, and Fisher [8] and adapted to our specific requirements. The algorithm for the fit is analytic, rather than iterative like the majority of its predecessors, and so is computationally inexpensive.

To begin with, a general conic section in two-dimensions can be represented as:

$$\mathbf{F}(\mathbf{a},\mathbf{x}) = \mathbf{a}\cdot\mathbf{x} = ax^2 + bxy + cy^2 + dx + ey + f = 0 \quad (3)$$

where $\mathbf{a} = \begin{bmatrix} a & b & c & d & e & f \end{bmatrix}^T$ and $\mathbf{x} = \begin{bmatrix} x^2 & xy & y^2 & x & y & 1 \end{bmatrix}^T$. $\mathbf{F}(\mathbf{a},\mathbf{x_i})$ then represents the algebraic distance of the point (x_i, y_i) to the conic defined by $\mathbf{F}(\mathbf{a},\mathbf{x}) = 0$. Minimizing the sum of the squares of these distances for all N data points, x_i, yields the equation:

$$D(\mathbf{a}) = \sum_{i=1}^{N} F(x_i)^2 \quad (4)$$

Now, in order to specifically fit an ellipse to the data instead of a general conic section, a constraint must be applied to the minimization problem. While numerous constraints have been proposed in the past [4] [10] [21], Fitzgibbon, Pilu, and Fisher set $4ac - b^2 = 1$, thus forcing the discriminant to be negative and creating an ellipse specific minimization. In matrix form this constraint takes the form $\mathbf{a^T C a} = 1$ where

$$C = \begin{bmatrix} 0 & 0 & 2 & 0 & 0 & 0 \\ 0 & -1 & 0 & 0 & 0 & 0 \\ 2 & 0 & 0 & 0 & 0 & 0 \\ 0 & 0 & 0 & 0 & 0 & 0 \\ 0 & 0 & 0 & 0 & 0 & 0 \\ 0 & 0 & 0 & 0 & 0 & 0 \end{bmatrix}$$

and the minimization problem becomes to minimize:

$$\mathcal{E} = \| \mathbf{Da} \|^2$$

subject to the above constraint, where $D = \begin{bmatrix} x_1 & x_2 & \dots & x_N \end{bmatrix}^T$ is the $n \times 6$ design matrix. Through the use of a Lagrangian variable λ and differentiation a simultaneous system of equations can then be obtained

$$\begin{aligned} 2\mathbf{Sa} &= \lambda \mathbf{Ca} \\ \mathbf{a^T Ca} &= 1 \end{aligned} \quad (5)$$

where $S = D^T D$. Thus, an eigensystem has been obtained which can be eaily solved. The final step is to note that the eigensystem actually yields 6 eigenvalue-eigenvector pairs, but as Fitzgibbon, Pilu, and Fisher prove, only one of these pairs will have a positive λ and therefore yield a true local minimum. For a more detailed discussion of the ellipse-specific fitting problem, please see [7] or [8].

Having obtained the fitted ellipses, we then calculate their geometric eccentricity which can be defined as the ratio of the semi-minor axis of the ellipse to the semi-major axis. This measure is in fact a two-dimensional cousin of the three-dimensional sphericity previously discussed, providing information on how well the rock approximates a circle.

The other metric which we obtained by fitting ellipses to the rock was the error of fit. This was calculated by summing the squared distance from each rock boundary point to the closest point on the ellipse. Due to the fact that finding the perpendicular ellipse-point distance required solving a higher order polynomial and as such was computationally expensive, we developed a slightly different distance measure. The distance between a data point and the ellipse was taken to be the distance between the data point and a point on the ellipse which rested on the ray originating from the ellipse center and passing through the data point (Figure 2). This method of calculating the ellipse-point distance allowed us to use a purely analytic method of distance calculation and not have to revert to iterative method's such as the Gauss-Newton process.

Roundness Calculation – The roundness of each rock was next obtained, again using only the boundary points obtained through segmentation and the simple edge-finding technique. The general concept of our roundness measure is based upon

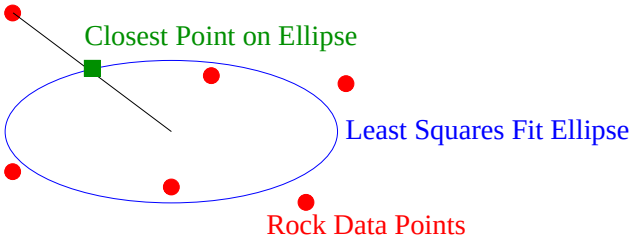

Figure 2: The distance between a data point and a fit ellipse is shown calculated along a ray emanating from the ellipse's center and passing through the data point.

the algorithm developed by [5] to detect corners of high-angularity in images.

Assuming the boundary points are labelled in the clockwise direction starting from some arbitrary point, we wish to estimate the curvature at a particular point P_i. To do this, numerous triangles are fit with the apex of each triangle resting at P_i. The two remaining vertices of the triangle are positioned one to either side of P_i and are moved to various distances. Thus, we have points P_h and P_j, where for two predefined integer constants α and β

$$\begin{array}{ll} h < i - \alpha & j > i + \alpha \\ h > i - \beta & j < i + \beta \end{array}$$

After some early experimentation, it was found that if α was set to 2 and β was set to 9, the most useful results could be obtained.

For all possible combinations of h and j within these constraints, the angle $\angle$hij was then calculated using the Law of Cosines:

$$\angle hij = \arccos \frac{a^2 + b^2 - c^2}{2ab} \tag{6}$$

with $a = \| P_h - P_i \|$, $b = \| P_j - P_i \|$, and $c = \| P_h - P_j \|$. Point P_i's estimated curvature was then taken to be the maximum possible $\angle hij$ for all possible h and j (Figure 3).

Having found an estimated curvature, ρ_i, at every point on the boundary, we next examined the distribution of these values. We defined the final roundness of each rock as the standard deviation of the estimated curvature at each point. Thus for a rock with N boundary points:

$$\mathcal{R}_{2d} = \sqrt[2]{\frac{1}{N-1} \sum_{i=1}^{N} (\rho_i - \bar{\rho})^2} \tag{7}$$

with $\bar{\rho}$ equal to the average of the curvature at the N points.

This measure provided a relative angularity scale. For instance, a perfectly round, circular object would rate a zero on this roundness scale, while any deviations, points, or jagged edges would serve to increase the rock's roundness. Thus, the greater a rock's roundness in terms of our measure, the more angular and rough its edges could be said to be.

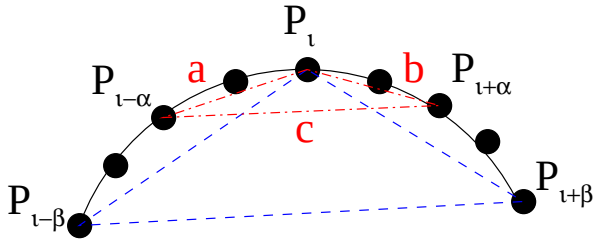

Figure 3: The calculation of the estimated curvature at point P_i is shown. Triangles are inscribed using P_i as one of the vertices and points between $P_i \pm \alpha$ and $P_i \pm \beta$ as the other two. The maximum possible vertex angle is taken to be the estimated curvature at P_i.

Three Dimensional Shape Characterization

After completing the two-dimensional analyses, our next step was to implement similar methods for the more complex three dimensional case (Figure 6). Once again our procedure began by segmenting the rocks from the background image. Then using the topographical-like data obtained through the plane-fitting method described above, an ellipsoid was fit to the points in three dimensions. An analytic solution to this problem was not feasible, so we implemented an iterative minimization solution to the least squares fitting problem. After the ellipsoid was fit and the sphericity and other measures were acquired from it, the data was next approximated with a b-spline surface. This surface provided the continuity necessary for the calculation of the second derivatives of the data, providing us with a novel metric for the three-dimensional relative angularity of the rock.

Ellipsoid Fitting – Unable to suitably generalize to three-dimensions the ellipse-specific fitting method utilized for the two-dimensional shape characterizations, we turned instead to an iterative solution. After researching the merits and limitations of several different techniques [16] [22] [23], we finally settled on a form of Powell minimization [19], which appeared to be the least computationally time-consuming technique and the most aptly suited to the data we had available.

The backbone of Powell's method for multidimensional function minimization is actually the one-dimensional minimization procedure known as Brent's method or inverse parabolic interpolation. To utilize Brent's method, an initial coarse bracketing of the minimum is first accomplished through a naive downhill searching algorithm (Figure 4). This simple search ensures that a minimum is located between the three abscissa points, a, b, and c, which are its output. The key assumption of Brent's method is that given a sufficiently smooth and continuous function, it will most likely behave much like

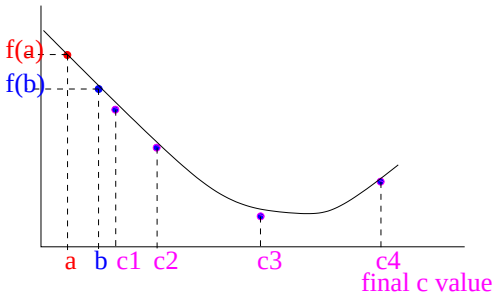

Figure 4: The figure depicts the initial coarse bracketing of a function minimum. Points a and b are first randomly chosen, and increasing c values are then guessed in a downhill direction until the function stops decreasing and begins to increase.

a parabola near the minimum. As such, if three points are fit to a parabola, in this case those points initially being the $f(a)$, $f(b)$, and $f(c)$ calculated above, the minimum of that parabola should be extremely close to the minimum of the function. Using this concept, as well as a more naive but robust simple golden section search [19], Brent's method is able to narrow in on the function minimum up to an arbitrary precision.

As such, all that is required of Powell's method is to choose the directions of minimization in a way which requires the smallest possible number of iterations. This is accomplished through the use of conjugate directions which Powell first understood and implemented [19]. Powell's method then simply iterates, calling Brent's method to minimize the function in these conjugate directions until a multidimensional function minimization is accomplished.

In our particular case of ellipsoid fitting, two different distance metrics to minimize were implemented. The first of these, known as $\mathcal{D}_S$ was simply the sum of the squared distances from the rock data points $x_1, x_2, \ldots x_N$ to the closest point on the prospective ellipsoid $e_1, e_2, \ldots e_N$:

$$\mathcal{D}_S = \sum_{i=1}^{N} \parallel x_i - e_i \parallel^2 \tag{8}$$

As in the two-dimensional case, the point e_i was estimated by finding the intersection of the ellipsoid and the ray originating from the center of the ellipsoid and passing through the data point x_i. This, again, was done in order to increase computational efficiency and to utilize an analytic distance rather than one which would require iteration.

The second distance implemented was the bidirectional Hausdorff set difference. This metric is much used in image processing tasks [12] [17] and is considered a powerful tool for finding the distance between two sets of points. The Haus-

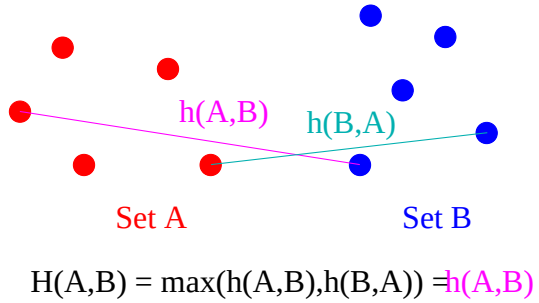

Figure 5: The Hausdorff distance between two sets, $H(A, B)$. This distance is often used in image processing tasks, and was here considered as a distance metric for the ellipsoid fitting.

dorff distance *from* set A *to* set B is defined as

$$h(A, B) = \max_{a \in A}(\min_{b \in B} \parallel a - b \parallel) \tag{9}$$

This is the unidirectional Hausdorff distance. The bidirectional version which tells the distance *between* two point sets (Figure 5) is simply defined as:

$$\mathcal{D}_H = \max(h(A, B), h(B, A)); \tag{10}$$

Both distance metrics held particular advantages to our task. Since we had at most semi-spherical data, being that surface of the rock which was facing the camera, the Haussdorff distance would attempt to fit an ellipsoid enclosing this surface. The data points would be somewhere near the center of the ellipsoid. This would enable us to fit an entire ellipsoid to the data and obtain reasonably good estimations of its three-dimensional axes. The sum of the squares distance on the other hand would fit one face of the ellipsoid to the rock and then interpolate where the rock might have been, fitting an ellipsoid much larger than the area of the actual data points. However, the part of the ellipsoid which was actually nearest to the data points would be fit directly to them and would achieve an effect much more like that used in the two-dimensional characterizations. For this reason, for its faster computation time, and due to the fact that the sum of the squares distance provided a better idea of the data's true shape, the metric first described was chosen.

Thus, an ellipsoid was fit to the data points by applying Powell's method to minimize the sum of the squared distance between the rock data points and the ellipsoid. Nine parameters were used to define the ellipsoid as per the parametric equation:

$$\begin{bmatrix} x \\ y \\ z \end{bmatrix} = R_1 R_2 R_3 \begin{bmatrix} a\cos(u)\cos(v) \\ b\sin(u)\cos(v) \\ c\sin(v) \end{bmatrix} + \begin{bmatrix} D \\ E \\ F \end{bmatrix} \tag{11}$$

where $-\pi \leq u \leq \pi$, $-\pi/2 \leq v \leq \pi/2$. The parameters a, b, and c define the semi-major, semi-intermediate, and semi-minor ellipsoid axes respectively while (D, E, F) represents

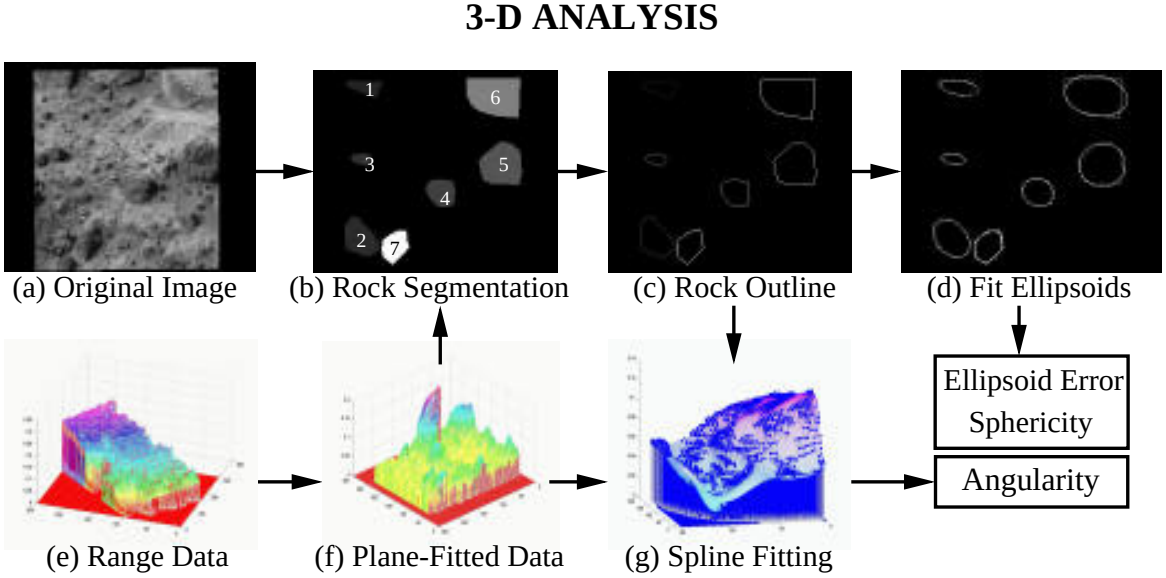

Figure 6: A flow chart of the three-dimensional analysis of an image $(\mathbf{a})$ is depicted. The process begins with the segmentation of the rocks from the image background $(\mathbf{b})$ with the help of the plane-fitted range data $(\mathbf{f})$. Outlines of the rocks are then found via edge detection $(\mathbf{c})$. B-splines are next fit to the range data $(\mathbf{g})$, and from these, angularity is calculated. Ellipsoids are also fit to the range data using a Powell minimization technique $(\mathbf{d})$. Finally, the sphericity and ellipsoid fitting error are calculated using the fitted ellipsoids. The entire process requires less than five minutes per image running in unoptimized Matlab code.

the center point of the ellipsoid. The matrices R_1, R_2, and R_3 are three-dimensional rotation matrices:

$$R_1 = \begin{bmatrix} \cos(\theta_1) & \sin(\theta_1) & 0 \\ -\sin(\theta_1) & \cos(\theta_1) & 0 \\ 0 & 0 & 1 \end{bmatrix}$$

$$R_2 = \begin{bmatrix} \cos(\theta_2) & 0 & \sin(\theta_2) \\ 0 & 1 & 0 \\ -\sin(\theta_2) & 0 & \cos(\theta_2) \end{bmatrix}$$

$$R_3 = \begin{bmatrix} 1 & 0 & 0 \\ 0 & \cos(\theta_3) & -\sin(\theta_3) \\ 0 & \sin(\theta_3) & \cos(\theta_3) \end{bmatrix}$$

where θ_1, θ_2, and θ_3 are the final three ellipsoid parameters specifying the angles of rotation of the ellipsoid about the z, y, and x-axes, respectively. It should be noted that the rotation of the ellipsoid occurs in that order.

Two metrics were derived from the ellipsoid fit. The first of these was the ellipsoid fitting error, being the averaged sum of the squared distance from each point on the rock to the ellipsoid, again using the estimated method for the calculation of the closest point on the ellipsoid. This metric provided a coarse estimate of the angularity of the rock. If the ellipsoid error was 0, the rock would then be a smooth faced ellipsoid or section thereof. However, as the rock's surface becomes more textured, as there are more bumps and indentations, the smooth ellipsoid surface would tend to fit less perfectly. As such high ellipsoid fitting errors can serve as an indication of rough or angular rocks.

The second piece of information measured using the ellipsoid fit was the rock's sphericity. This value was calculated using the formula given in equation 2, where d_L, d_I, and d_S have been replaced by the ellipsoid parameters a, b, and c, respectively. A sphericity of 1 in this case would indicate that the ellipsoid which was fit to this rock was perfectly spherical, and thus that the rock's surface itself was an exact approximation of a spherical section. As the sphericity falls farther from 1, the rock then takes on a more elongated shape in one or another direction. This information, as stated before, can then be used to determine how far the rock might have travelled in a flowing fluid [15].

Spline Fitting – The next step of our three-dimensional shape characterization was to calculate a more robust estimate of the roundness or angularity of the rocks. Our approach for determining roundness involved obtaining the derviatives and second dervivatives in various directions of the data representing the rock surface. Unfortunately, the calculation of such derivatives for our noisy range data using typical direction-step methods soon proved unreliable. Values were too often rendered useless by noise, and inaccuracies proved common. However, the fitting of b-splines to the data points via techniques derived in [20] smoothed the surfaces sufficiently that derivatives could then be calculated in an accurate and analytic method.

B-spline surfaces (Figure 7) are the two-dimensional cousins of b-spline curves which, along with Bezier curves, have become extremely important in computer graphics and design applications. In general the equation for drawing a b-spline

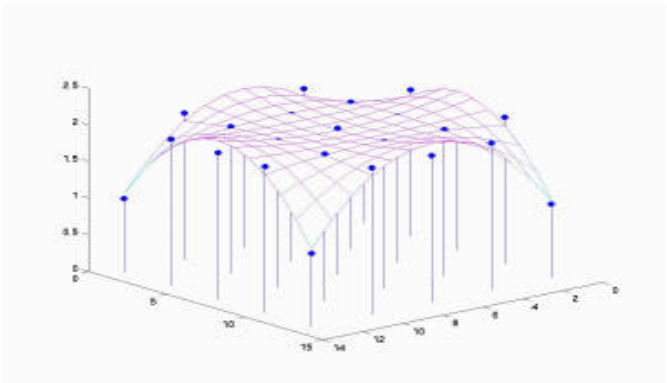

Figure 7: An example of a very simple B-spline surface. The spline is being fit to the stemmed data points using the method described below.

surface is:

$$Q(u,w) = \sum_{i=1}^{n+1} \sum_{j=1}^{m+1} B_{i,j} N_{i,k}(u) M_{j,l}(w) \qquad (12)$$

Here u and w are normalized paramtric directions. $Q(u,w)$ is the height of the surface at the particular parametric points. B is the $m \times n$ matrix containing the polygon net vertices, and $N_{i,k}(u)$ and $M_{j,l}(w)$ are the b-spline basis functions in the respective parametric directions. The CoxdeBoor recursive formula [20] defines these basis functions:

$$N_{i,1}(t) = \begin{cases} 1 & \text{if} \quad x_i \le t \le x_{i+1} \\ 0 & \text{otherwise} \end{cases}$$

$$N_{i,k}(t) = \frac{(t - x_i) N_{i,k-1}(t)}{x_{i+k-1} - x_i} + \frac{(x_{i+k} - t) N_{i+1,k-1}(t)}{x_{i+k} - x_{i+1}}$$

where x in this case is a knot vector and corresponds in no way to the data points. The development of the knot vectors will be discussed below. Calculation of the basis functions in the w direction proceeds via the equation above modulo the proper obvious substitions.

The general principle behind the construction of b-spline surfaces involves the definition of a net of polygon vertices. These vertices are evenly spaced in the two parametric directions, in our case simply the x and y axes in the image. The height at each net vertex determines the shape of the surface in and around that region. A surface is fit to this polygon net via interpolation. Bezier and b-spline surfaces differ only in the set of basis functions which are used to make this interpolation, and indeed, the Bezier basis functions, known as the Bernstein basis functions, are actually a degenerate set of the more general and versatile b-spline basis functions. The constants k and l define the order of the polynomial that is to be fit to the surface in the u and w parametric directions, respectively [20].

To calculate the b-spline surfaces for a rock, we first had to discern the polygon net which would have produced a b-spline passing through our actual data points. Assuming we have an $r \times s$ rectangular grid of three-dimensional data points and we wish to find the best-fitting $m \times n$ rectangular polygon net which could have produced those data points, we must invert a certain matrix form of the b-spline equation, namely:

$$\mathbf{D} = \mathbf{CB} \qquad (13)$$

In this equation $\mathbf{D}$ corresponds to $\mathbf{Q}$ in Equation 12 and is an $r * s \times 3$ matrix of the three-dimensional coordinates of the actual rock data points. B is now an $m * n \times 3$ matrix containing the coordinates of the polygon net vertices. C is an $r * s \times n * m$ matrix containing the products of the b-spline basis functions, N and M. With some longwinded manipulation it could be shown that Equation 12 and Equation 13 are indeed equivalent [20].

So, if $\mathbf{C}$ is a square matrix, the inversion process is simple and $\mathbf{B}$ can be found by:

$$\mathbf{B} = \mathbf{C^{-1}D} \qquad (14)$$

However, in the more general case where $\mathbf{C}$ is not square, a solution for $\mathbf{B}$ can only be obtained in some estimated sense. The standard inversion process in this case is:

$$\mathbf{B} = (\mathbf{C^T C})^{-1} \mathbf{C^T D} \qquad (15)$$

Once the polygon net vertices have been calculated, a b-spline which approximates the shape of the rock surface can then be drawn using Equation 12.

The purpose of fitting the splines was not to obtain the surfaces themselves, but rather their derivatives. There exists a relatively simple method of calculating the derivatives of the fitted surface in the two parametric directions once the polygon net matrix B has been obtained. In fact the derivatives can be found by simple partial differentiation. Thus, the second derivatives with which we are concerned would be:

$$\begin{aligned} Q^{uu}(u,w) &= \textstyle\sum_{i=1}^{n+1} \sum_{j=1}^{m+1} B_{i,j} N_{i,k}''(u) M_{j,l}(w) \\ Q^{ww}(u,w) &= \textstyle\sum_{i=1}^{n+1} \sum_{j=1}^{m+1} B_{i,j} N_{i,k}(u) M_{j,l}''(w) \end{aligned} \qquad (16)$$

Our angularity or roundness measure was based upon these derivatives. We took the average of the two derivatives at each point and found the mean of that for all points on the rock. Thus for N data points:

$$\mathcal{R}_{3d} = \frac{1}{N} \sum_{i=1}^{N} \frac{(Q_i^{uu} + Q_i^{ww})}{2} \qquad (17)$$

This metric provides one number which represents the roughness of the rock's surface. A score of zero would indicate that

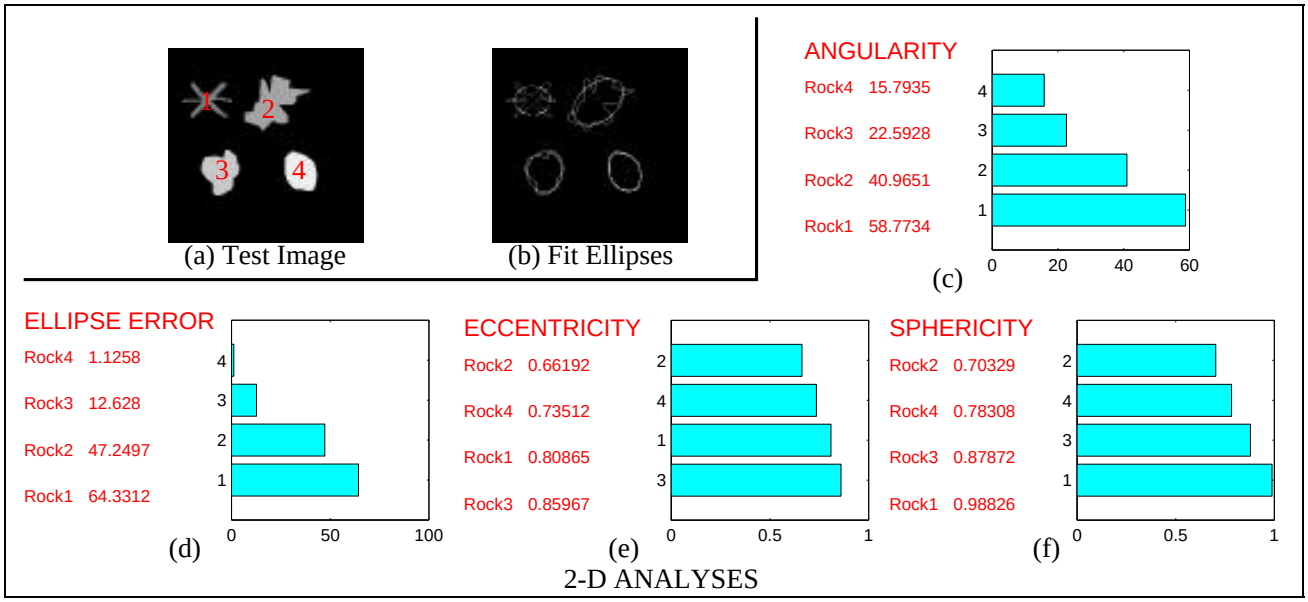

Figure 8: $(\mathbf{a})$ A hand-drawn image. It was designed to demonstrate the full-spectra of angularity and proceeds from greatest angularity (shape 1) to least (shape 4). $(\mathbf{b})$ An image depicting the ellipses that were fit to the four shapes. The results surrounding the images, $(\mathbf{c})$, $(\mathbf{d})$, $(\mathbf{e})$, and $(\mathbf{f})$, are of tests conducted on image $(\mathbf{a})$ using the four two-dimensional metrics developed in this paper.

the object is perfectly smooth and spherical, for the second derivative, which represents the change in the curvature of the surface, would be 0. As bumps, or rough edges appear on the rock, there will be greater and greater changes in curvature on average, and thus the rock's angularity will increase according to this measure.

3. Results

2-D Test Images

As stated, our methods were first applied in two-dimensions to a number of test images specifically hand-designed to demonstrate the principles of our metrics. Various images were created emphasizing either the two roundness measures, namely the angularity and the ellipse fitting error, or the two "sphericity" measures, being the eccentricity of the fit ellipses and the aspect ratio that we dubbed "2-D sphericity."

Roundness Test – A hand-designed image, along with the results of its analysis, is depicted in Figure 8. The shapes in the image were designed to proceed visually from highly angular to nearly round. Figure $8(\mathbf{c})$ shows that this trend is reflected in the angularity measure. The high incidence of sharp corners in the first shape combined with the existence of long flat regions makes for a very widespread distribution of inscribable angle values. Thus, the angularity measure was driven up to 58.7734. Shape 1 on the other hand consists of much smoother curves, most of which have similar degrees of curvature, granting it a very narrow distribution of inscribable angle values and thus a relatively low angluarity score of 15.7935. The measure not only provides a relative ranking, but also gives an idea of the similarities between shapes. As was to be expected by visual inspection, shapes 3 and 4 were perceived as being much more similar in angularity than, for instance, shapes 1 and 2.

The ellipse fitting error measure concurred with the angularity measure, displaying the obvious trend (Figure $8(\mathbf{d})$). An ellipse fit to a rounded shape should clearly not create as great an error as one fit to an extremely angular shape replete with jagged edges and corners. Thus, shape 4's ellipse was fit with a total error of only 1.1258 while the ellipse fit to shape 1 exhibited a much greater error of 64.3312. This measure also provides information about the similarity between shapes. Once again supporting the angularity measure, shapes 3 and 4 showed errors more similar to one another than did shapes 1 and 2.

Sphericity Test – An image specifically created to demonstrate the accuracy of the two sphericity measures is depicted in Figure 9 along with its analysis. The image was crafted to proceed from a highly oblong shape to a nearly circular one. This trend was accurately perceived by the 2-D sphericity measure (Figure $9(\mathbf{f})$). The measure, essentially a measure of the shape's aspect ratio, was a mere 0.19332 for the thin and narrow shape 1, but reached 0.95204 for shape 4. This latter number being so near to one indicated that shape 4 was almost perfectly circular. The measure determined not only a relative ranking of the shape's 2-D sphericities, but also a concrete measure of their similarities to one another. The first two shapes are much more alike to each other than

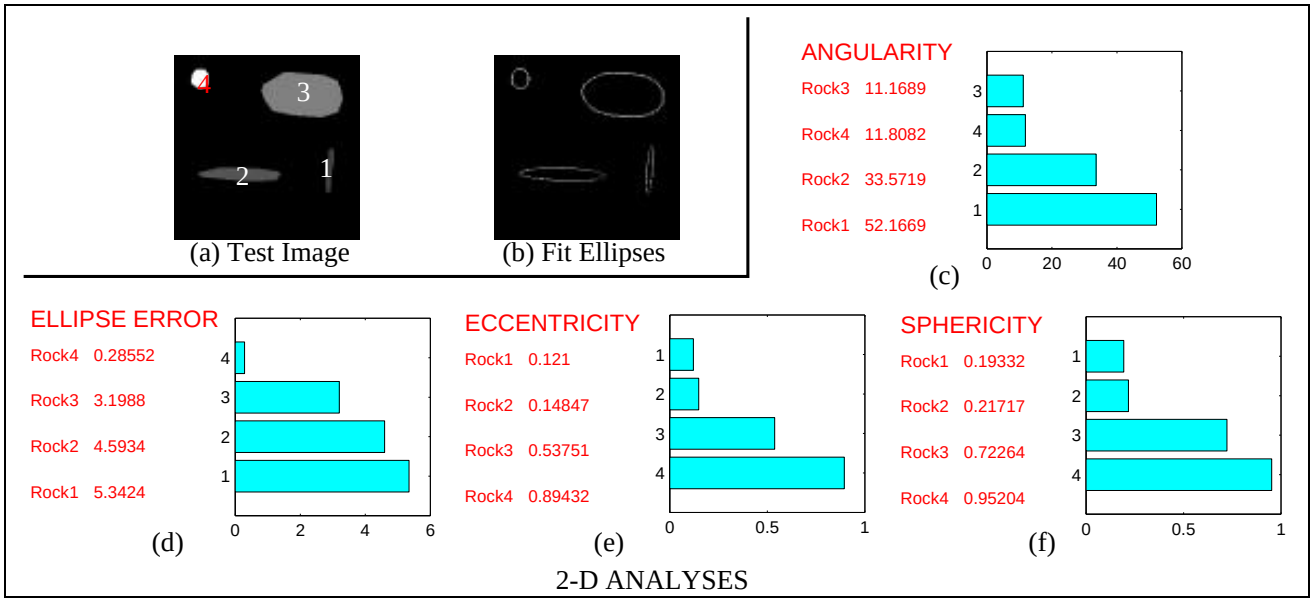

Figure 9: (**a**) A hand-drawn image. It was designed to demonstrate the full-spectra of two-dimensional sphericity and proceeds from least sphericity (shape 1) to greatest (shape 4). (**b**) This image depicts the ellipses that were fit to the four shapes. The results surrounding the images, (**c**), (**d**), (**e**), and (**f**), are of tests conducted on the image (**a**) using the four two-dimensional metrics developed in this paper.

they are to the final two, and this is indicated by the fact that shape 1 and shape 2 are separated from each other by only 2.4 percent of the measure's range, while shape 2 is separated from shape 3 by over 50 percent of the measure's range.

The eccentricity of the fit ellipses also gave an indication of the desired trend (Figure 9(**e**)). Shape 1 exhibited a low 0.121 while the circular shape 4 exhibited a much greater 0.89432. As with the other measures, similarity between shapes can be determined using the eccentricity of the ellipses. Shape 1 and shape 2 are separated from each other by only 2.7 percent of the measure's range while shape 2 and shape 3 are separated by almost 39 percent of the range.

Consistency Across Views

After demonstrating the measures on synthetic images, we applied them to real world images. In this experiment, we wished to determine the behavior of the measures for images of the same set of rocks taken from different viewpoints.

For this task, we used a series of images (Figure 10) containing three rocks found in JPL's Mars Yard taken from different viewing angles. Steroe pairs of images were taken, and therefore range data was available upon which three-dimensional techniques could also be applied. We present here only the results of the three roundness-type measures.

What can be observed from Tables 1, 2, and 3 is that these measures determine trends in angularity among real world images. All measures indicate that rock 1 was the most

Table 1: The two-dimensional angularity results measured on the four images shown in Figure 10.

2-D Angularity			
——	ROCK 1	ROCK 2	ROCK 3
VIEW 1	23.05	13.40	10.39
VIEW 2	14.71	13.93	11.71
VIEW 3	17.42	16.68	12.78
VIEW 4	15.65	10.34	9.60

Table 2: The two-dimensional ellipse fitting error results measured on the four images shown in Figure 10.

2-D Ellipse Fitting Error			
——	ROCK 1	ROCK 2	ROCK 3
VIEW 1	34.16	13.71	5.98
VIEW 2	13.36	10.65	3.60
VIEW 3	17.31	15.98	3.72
VIEW 4	10.34	5.65	1.89

angular of the three, followed by rock 2 and then rock 3. Both of the two-dimensional measures, as well as the three-dimensional angularity measure, exhibited this trend which is evident from visual inspection.

Furthermore, what can be seen in the tables is that the measures were able to identify this trend regardless of the angle from which the image was taken and in what position or order the rocks were situated. Rock 1 is clearly much more angu-

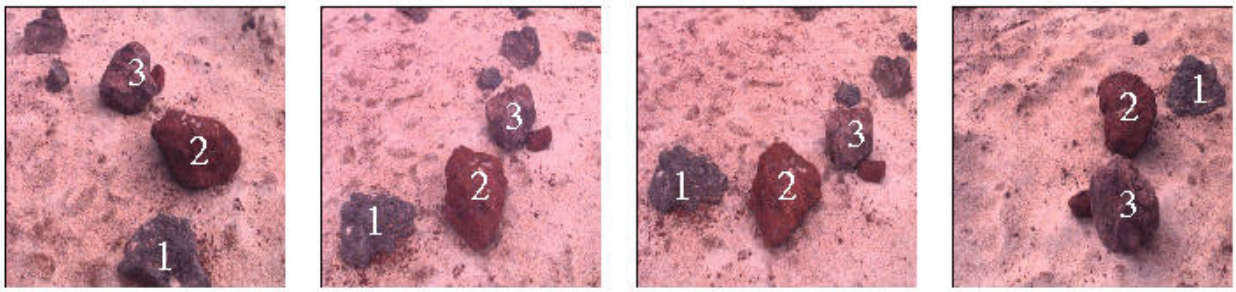

Figure 10: These four images were taken using two stereo-mounted digital cameras in the JPL Mars yard. All four images depict the same three rocks, each image differing only in camera angle. Tests were conducted on these four images to test the consistency of the developed metrics. Visually, the rocks proceed in angularity from greatest (rock 1) to least (rock 3).

Table 3: The three-dimensional angularity results measured on three of the four images shown in Figure 10.

3-D Angularity			
—	ROCK 1	ROCK 2	ROCK 3
VIEW 1	61.92	24.97	2.16
VIEW 3	11.06	6.08	1.34
VIEW 4	0.95	0.32	0.24

lar than the other two in every view and with regard to every measure while rock 3 is always the least angular.

One of the biggest disadvantages of the measures which can be seen in Table 3 is the variability between images viewed from different angles. While the techniques can rank various rocks and shapes within a single image according to their relative angularity, there is a great deal of variation in the absolute values of these measures between images taken from different angles. However, it is interesting to note that in this example the measures often remain stable relatively from image to image. That is, for instance, in Table 1 it can be calculated that from angle 2 rock 2 is 94.75 percent as angular as rock 1 while rock 3 is 79.65 percent as angular as rock 1. From angle 3, it can be shown that rock 2 is 95.74 percent as angular as rock 1 and rock 3 is 73.35 percent as angular as rock 1. The close correlation of these results may indicate that in some cases each rock is identified with similar relative angularity across images, but that merely the absolute values of the measures are fluctuating. Due to this fact, it is possible that the variability is being caused by some systematic variability among the images themselves. For instance, deeper shadows in some images may make rocks appear to be more angular and recessed than they would from other lighting angles. Rocks that are not symmetric would be expected to have different responses to shape measures when viewed from different angles, and this may account for the variability noted here. Despite this disadvantage, the measures provides a method by which the relative roundness of the rocks within an image can be catalogued.

Close Analysis of Two Sojourner Images

In our final experiment, we examined a number of Martian images returned by the Sojourner rover to determine how well our measures could perform on them. The analysis of two such images is described in detail here. A summary of the results for seven images is provided in the next section.

Image i1246925510l – The image in Figure 11$(\mathbf{a})$ is of a portion of the Martian Rock Garden near the Pathfinder landing site and features the noted rocks Flat Top, labelled 3, Little Flat Top, labelled 4, and Stimpy, labelled 5. Flat Top and Little Flat Top are both relatively smooth and box-like in appearance while Stimpy is much rougher and more angular in texture, though nearly circular in two-dimensional shape in this particular image.

First examining the two-dimensional analysis of these three particular rocks, it is seen that the two-dimensional roundness measures, the angularity and the ellipse fitting error, performed reasonably well. As can be seen from the segmentation image in Figure 11$(\mathbf{b})$, Stimpy (rock 5) has by far the smoothest outline according to the two-dimensional image, and so its angularity measure is a mere 12.1069. (Figure 11$(\mathbf{c})$) Flat Top (rock 3) and Little Flat Top (rock 4), on the other hand, have very jagged outlines and so their scores are more than double that of Stimpy. The ellipse fitting error results (Figure 11$(\mathbf{f})$) display the same relative ranking. The figures are extremely compelling in fact, with Stimpy measuring only 2.87 and Little Flat Top topping the list with a much greater 9.8382. This result indicates the squarish outlines of the two Flat Tops which created large errors when these 'square pegs' were fit with 'round holes.' It is interesting to note that these results are in line with the characterizations provided in [2].

The two-dimensional sphericity measures (Figures 11$(\mathbf{e})$ and 11$(\mathbf{g})$) also concurred in their findings in regard to the three rocks. Stimpy most resembles a circle as is shown by its greater score in both the eccentricity measure and the sphericity measure. Little Flat Top on the other hand was found at the bottom of the rankings due to its short, oblong appearance. Flat Top was so nearly square that its aspect ratio and the eccentricity of the ellipse that was fit to it were much closer to

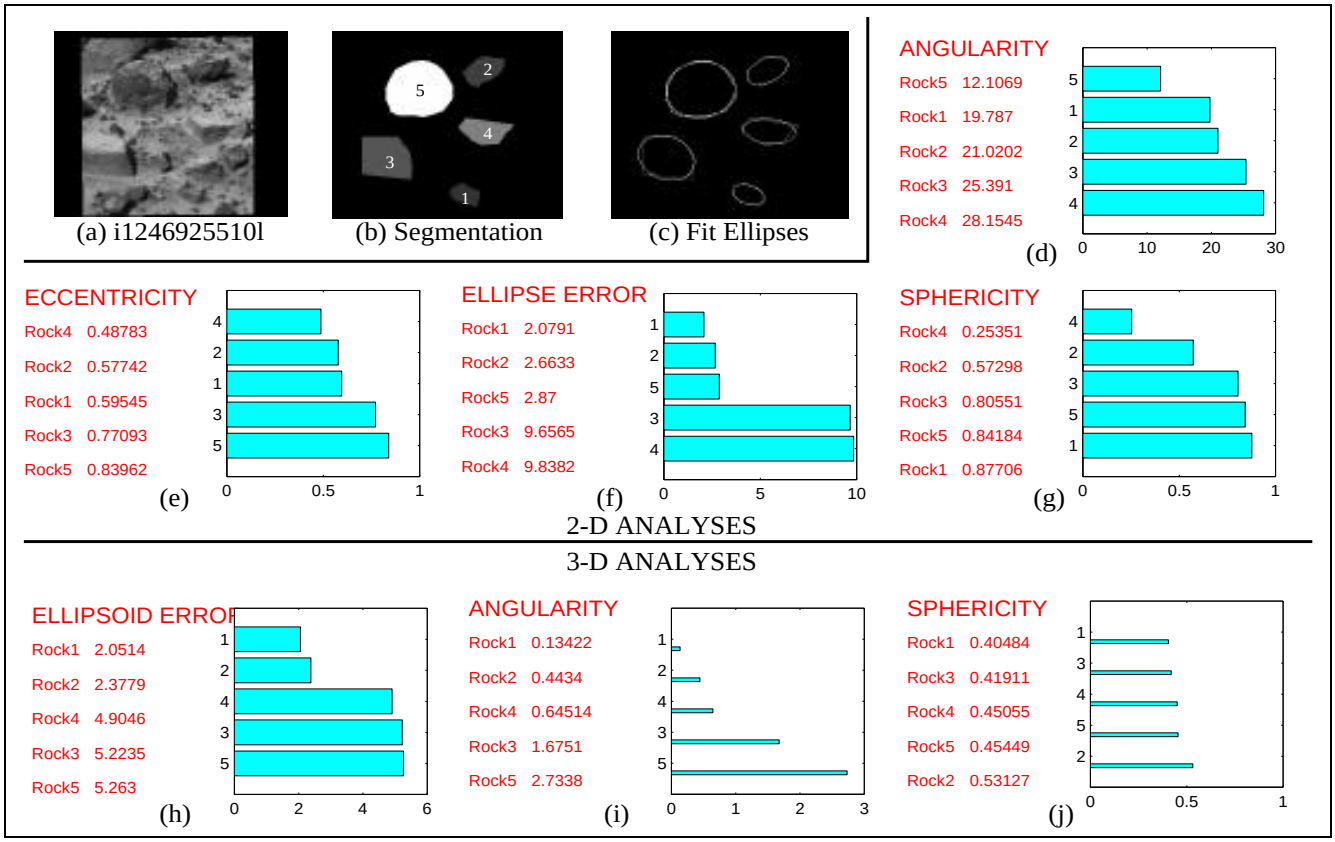

Figure 11: The first image shown here $(\mathbf{a})$ is taken from the Martian Rock Garden and features the rocks Flat Top, Little Flat Top, and Stimpy, rocks 3, 4, and 5, respectively. The second image $(\mathbf{b})$ is the adapted result of the rock segmentation procedure, and the third image $(\mathbf{c})$ shows the ellipses fit to the rocks. From the results surrounding the image, $(\mathbf{d}) - (\mathbf{j})$, it can be seen that the metrics were able to properly rank the three named rocks according to the seven different properties measured.

mimicking the round Stimpy than the oblong Little Flat Top.

In three dimensions, the measures also gave satifying results. The three-dimensional roundness measure, as was stated, attempts to measure fine scale features and roughnesses in the texture of the rock. As such, the relatively smooth Flat Tops exhibited lower three-dimensional angularity scores than the much rougher Stimpy whose peak is cracked and broken (Figures $11(\mathbf{h})$ and $11(\mathbf{j})$). Finally, the sphericity score again reflects the round, ballish nature of Stimpy and the squarish box-like nature of the Flat Tops. Stimpy has the highest sphericity score of the three (Figure $11(\mathbf{i})$).

It should be remarked here that the two-dimensional measures and the three dimensional measures often do not draw the same conclusions. This is not unexpected as the two techniques are working with different data and using different criteria. The two-dimensional angularity score rates the roughness of the outline of the rock segmented from the background image while the three-dimensional score rates the roughness of the surface of the rock gleaned from stereographically created range data. Two-dimensional sphericity is purely a measure of how circular the outline is opposed to three-dimensional sphericity which takes into account the spherical nature of the rock surface for which data is available.

Image i1246924795l – The image in Figure $12(\mathbf{a})$ was also taken in the Martian Rock Garden and features the rocks Bamm-Bamm, labelled rock 5 here, and Flute Top, labelled rock 6. Flute Top is a broad, low rock nearly rectangular in shape with a pocked, fluted surface. Bamm-Bamm on the other hand is a taller, more spherical rock with a highly pitted surface. The other rock that we will include in our discussion, we believe is unnamed. Rock 4 appears to be of a more oblong shape with a realtively smooth surface.

Beginning with the two-dimensional analysis, it can be seen that the roundness measures performed accurately. The outline of Flute Top with its almost 90 degree corner, its two flat sides (due to image edge effects unfortunately), and its one rounded arc scored much higher on both the angularity measure (Figure $12(\mathbf{d})$) and the ellipse fitting error measure (Figure $12(\mathbf{f})$. Bamm Bamm's outline contains a number of protrusions which gave it the second highest rankings of the three rocks. Rock 4's outline has no real corners and is rela-

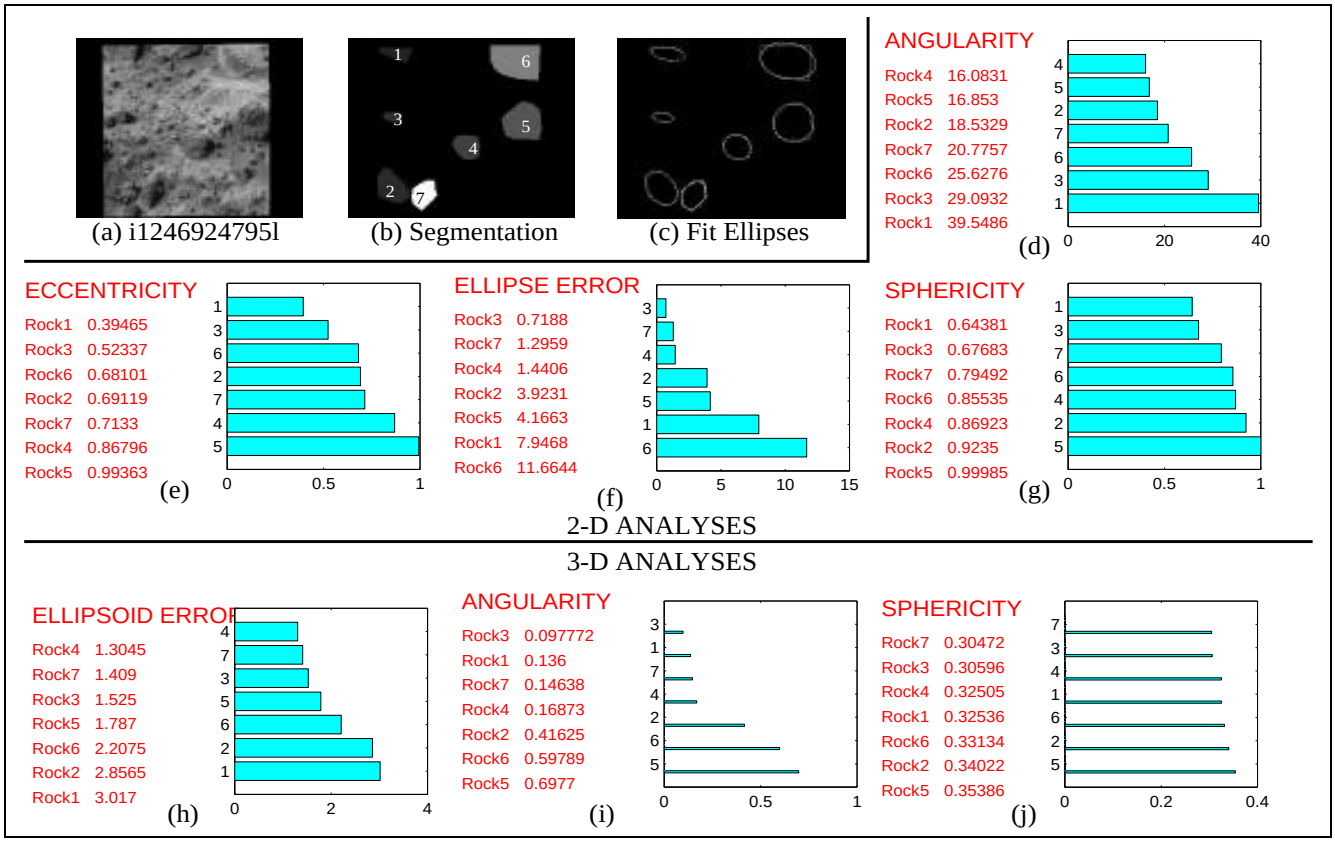

Figure 12: The first image shown here $(\mathbf{a})$ is taken from the Martian Rock Garden and features the rocks Bamm-Bamm and Flute Top, rocks 5 and 6, respectively. The second image $(\mathbf{b})$ is the adapted result of the rock segmentation procedure, and the third image $(\mathbf{c})$ shows the ellipses fit to the rocks. The results surrounding the images, $(\mathbf{d}) - (\mathbf{j})$, show that the metrics can be used rank the rocks in the image according to the desired properties.

tively smooth, and so it was correctly ranked lower than the other two rocks in both angularity and ellipse fitting error. The sphericity measures in two dimensions (Figures 12$(\mathbf{e})$ and 12$(\mathbf{g})$) further resulted in expected relatives values, with Flute Top being rated most oblong of the three rocks.

In three-dimensions, the textures of the three rocks are categorized well by the angularity measure (Figure 12$(\mathbf{i})$). Bamm-Bamm, as was said before, has very deep scars upon its surface and so was given the highest angularity score, 0.6977. Flute Top was a close second, its namesake flutes giving it a considerable score of 0.59789. Rock 4, of course, is generally smooth, and so its angularity was rated at a much lower 0.16873.

The Ellipsoid fitting errors (Figure 12$(\mathbf{h})$) for this image bear a moment's hesitation. It will be noticed that Flute Top is apparently ranked out of order by this measure. The reason for this is that the ellipsoid fitting error can best be used as a measure of angularity if it is assumed that a rock is in general a spheroid. Since the broad, low Flute Top is not a spheroid, it received error not only from the small surface deviations that we wished to measure, but from the fact that we were attempting to fit an ellipsoidal surface to a box-like one. In this respect, the ellipsoid fitting error may at times also be an indicator of sphericity. Aside from this anomaly, the ellipsoid fitting error did rank Rock 4 below Bamm-Bamm which was indeed a success, Bamm-Bamm being the rougher of the two.

Finally, upon examining the sphericity measure in three-dimensions (Figure 12$(\mathbf{j})$), it is seen that Bamm-Bamm received the highest score. Since it is the most spherical rock present, this was to be expected. Rock 4 on the other hand is noticably oblong, or football-shaped, and as such scored a much lower 0.32505 for this measure.

Larger Scale Experimentation

Having shown that the techniques perform well on the real world Mars images, the next task was to determine how the measures performed across a number of images. Figure 13 depicts seven of the Sojourner images that were experimented upon and Tables 4 and 5 present the summarized results of trials conducted on the seven selected images. A number of

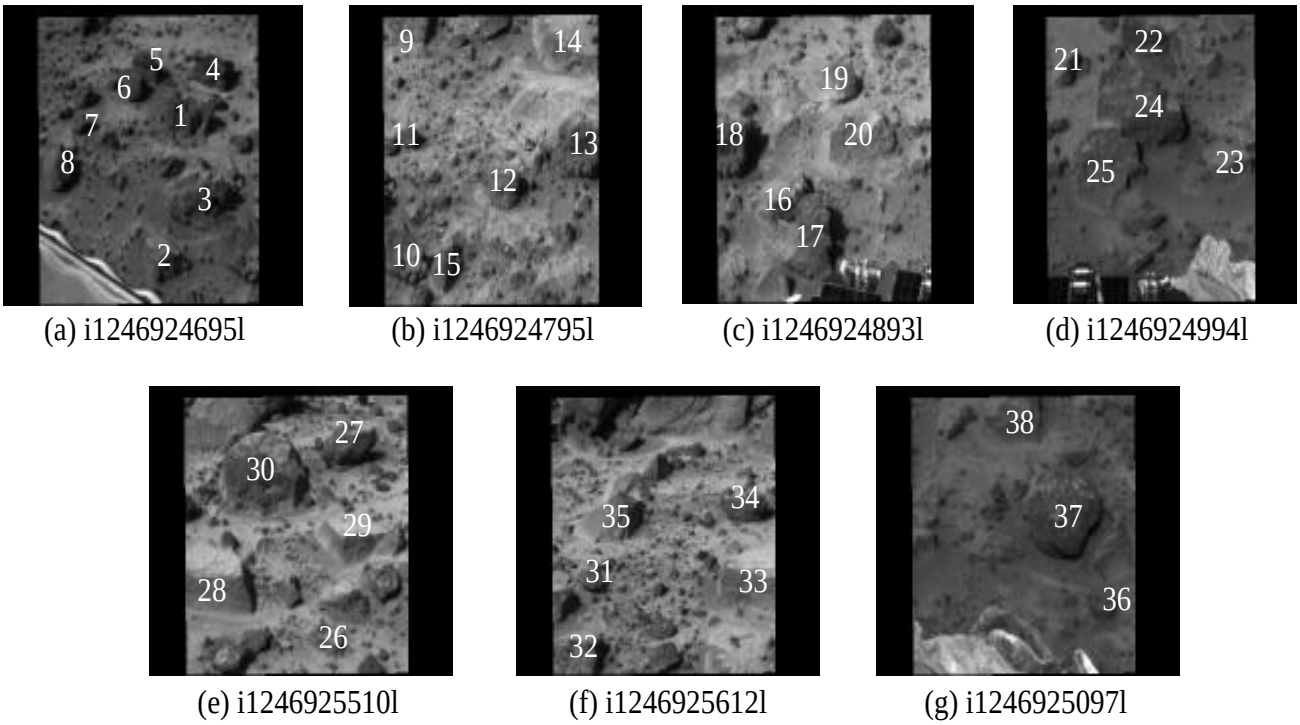

(a) i1246924695l (b) i1246924795l (c) i1246924893l (d) i1246924994l

(e) i1246925510l (f) i1246925612l (g) i1246925097l

Figure 13: The seven Sojourner images that we chose to analyze are depicted. The rocks used were randomly chosen and numbered for convenience. The images are of well-known areas in the Rock Garden near to Pathfinder's landing site.

comments are worth making with regards to these results.

First, the results of these trials appear logical when examined visually. For instance, Bamm Bamm (rock 18) appears much rougher than rock 20. This can also be seen in the results by comparing Bamm-Bamm's 0.609397 three-dimensional angularity score to rock 20's much lower 0.386075, a ranking also indicated by the two rocks' ellipsoid fitting error results, two-dimensional angularity results, and ellipse fitting error results. Other roundness comparisons could also be made, such as between rock 10 and rock 15 or between rock 25 and rock 3, which would also show the validity of these measures. Sphericity comparisons too, such as between rock 20 and rock 34 or between rock 25 and rock 27, show that this measure is capable of providing an accurate estimate of the property it was designed to measure.

Also, even though, as was previously discussed, there may sometimes be variation in the absolute magnitude of the measures from image to image due to uncontrolled conditions, many other times the measures are able to translate between two images. For instance, Bamm-Bamm appears in two different images as both rock 13 and rock 18. Even though the same exact portion of the rock does not appear in both images and as such the texture of the rock is not exactly the same, the three-dimensional angularity measures are very similiar (see rankings in Table 5). Table 5 provides another example of this when we look at the two entries for Flat Top. Flat Top appears in two images as rock 28 and rock 33, and these two rocks are found right beside each other when the rocks are ranked in order of increasing 3-D angularity.

4. Conclusions

In attempting to develop a technique by which an automated rover could quantifiably classify the shape of a rock, seven different metrics were designed and implemented. In two dimensions, a novel angularity measure was developed which was augmented by a second measure, the ellipse fitting error. These two combined were able to rank the relative roundness of the rocks in an image each with a single quantifiable value. Two metrics were also developed for two-dimensional "sphericity" which both provided quantifiable information about a rock's shape. In three dimensions, b-splines were fit to stereographic range data, and the second derivatives of these surfaces were calculated in order to obtain a single value which characterized the roughness of a rock's surface. This measure, too, was augmented by a measure of the error incurred when fitting an ellipsoid to the range data which yielded another method by which rock shape could be categorized. Finally, the approximate three-dimensional sphericity of the rock was calculated by using the axes of the ellipsoid which most closely approximated the data, giving one final piece of information about the rock's morphology.

Table 4: This table shows the results of experiments conducted on the seven selected Martian Rock Garden images. A total of 38 rocks were chosen, and all seven metrics developed in this paper were applied to each rock.

Rock	Eccentricity	Ellipse Error	2-D Spher.	2-D Angularity	Ellipsoid Error	3-D Spher.	3-D Angularity
1	0.77	4.77	0.94	25.36	2.25	0.35	0.42
2	0.61	10.83	0.82	23.38	1.89	0.68	0.66
3	0.76	7.68	0.84	19.25	2.40	0.39	0.82
4	0.60	1.71	0.69	17.53	1.42	0.48	0.31
5	0.60	1.41	0.86	18.62	2.08	0.34	0.11
6	0.59	2.65	0.75	22.72	1.34	0.39	0.04
7	0.50	0.30	0.54	32.23	1.22	0.28	0.03
8-Geordi	0.70	1.85	0.79	19.24	0.89	0.44	0.20
9	0.39	7.95	0.64	39.55	3.02	0.33	0.14
10	0.69	3.92	0.92	18.53	2.86	0.34	0.42
11	0.52	0.72	0.69	29.09	1.53	0.31	0.10
12	0.87	1.44	0.87	16.08	1.30	0.33	0.17
13-Bamm-Bamm	0.99	4.17	1.00	16.85	1.79	0.35	0.70
14-Flute Top	0.68	11.66	0.86	25.63	2.21	0.33	0.60
15	0.71	1.30	0.79	20.78	1.41	0.30	0.15
16	0.66	18.05	0.70	25.41	2.55	0.40	0.32
17	0.54	13.42	0.76	22.14	6.22	0.56	2.63
18-Bamm-Bamm	0.76	13.54	0.92	29.21	1.92	0.41	0.61
19	0.70	1.07	0.76	16.69	3.75	0.37	0.22
20	0.63	7.45	0.61	19.91	1.80	0.30	0.39
21	0.49	0.39	0.58	23.67	2.07	0.43	0.47
22	0.52	1.38	0.70	17.59	3.44	0.40	0.19
23	0.59	1.92	0.72	18.35	3.40	0.39	0.18
24-Garrak	0.51	7.75	0.65	11.20	4.21	0.34	1.93
25	0.82	8.61	0.93	24.36	1.98	0.25	0.45
26	0.60	2.08	0.88	19.79	2.05	0.40	0.13
27	0.58	2.66	0.57	21.02	2.38	0.53	0.44
28-Flat Top	0.77	9.66	0.81	25.39	5.22	0.42	1.68
29-Lil Flat Top	0.49	9.84	0.25	28.15	4.90	0.45	0.65
30-Stimpy	0.84	2.87	0.84	12.11	5.26	0.45	2.73
31	0.84	2.30	0.78	25.13	0.89	0.47	0.08
32	0.83	2.90	0.96	19.77	0.99	0.35	0.14
33-Flat Top	0.97	12.94	0.97	28.30	2.74	0.51	1.32
34	0.46	4.15	0.46	25.79	2.54	0.46	0.34
35	0.48	2.87	0.48	18.76	5.18	0.45	0.45
36	0.70	3.84	0.52	31.61	1.59	0.28	0.08
37-Grommit	0.97	3.97	1.00	10.29	2.73	0.33	2.98
38-Mohawk	0.75	4.63	0.77	23.28	2.99	0.38	0.77

Table 5: The 38 Martian Rock Garden rocks from the seven selected images are here ranked in order of increasing 3-D angularity.

Rock	3-D Angularity
7	0.029
6	0.044
31	0.080
36	0.083
11	0.098
5	0.109
26	0.134
9	0.136
32	0.144
15	0.146
12	0.169
23	0.184
22	0.191
8	0.202
19	0.217
4	0.312
16	0.315
34	0.341
20	0.386
10	0.416
1	0.422
27	0.443
25	0.450
35	0.452
21	0.473
14	0.598
18	0.609
29	0.645
2	0.657
13	0.698
38	0.769
3	0.822
33	1.321
28	1.675
24	1.929
17	2.628
30	2.734
37	2.977

When utilized together, the techniques developed may provide a powerful tool to help future automated rovers to not only see the surface of a planet, but to understand it. This in turn could aid in the prioritization of data collection and downlinking which would serve to increase mission productivity and scientific return.

ACKNOWLEDGEMENTS

The authors would like to thank Wolfgang Fink for his useful discussions and, in particular, his suggestions on spline fitting and Eric Mjolsness for his helpful ideas on distance metrics. The research described in this paper was funded by the Remote Exploration and Experimentation Project and by the Cross-Enterprise Technology Development Program and was carried out at the Jet Propulsion Laboratory, California Institute of Technology, under a contract with the National Aeronautics and Space Administration.

REFERENCES

[1] ASTM, "Standard Test Method for Flat Particles, Elongated Particles, or Flat and Elongated Particles in Coarse Aggregate," 1995.

[2] A. T. Basilevsky, W. J. Markiewicz, N. Thomas, and H. U. Keller, "Morphologies of Rocks Within and Near the Rock Garden at the Mars Pathfinder Landing Site," *Journal of Geophysical Research*, **104**(E4), pp. 8617-8636, 1999.

[3] H. Blatt, G. Middleton, and R. Murray, *Origin of Sedimentary Rocks* Prentice-Hall Inc., 434 pp., 1972.

[4] F. L. Bookstein, "Fitting Conic Sections to Scattered Data," *Computer Graphics and Processing*, **9**, pp. 56-71, 1979.

[5] D. Chetverikov and Z. Szabo, "Detection of High Curvature Points in Planar Curves," *Proc. 23rd Workshop of the Austrian Pattern Recognition Group*, pp.175-184, 1999.

[6] G. Dudek and J. K. Tsotsos, "Shape Representation and Recognition from Multiscale Curvature," *Computer Vision and Image Understanding*, **68**(2), pp. 170-189, 1997.

[7] A. W. Fitzgibbon, M. Pilu, and R. B. Fisher, "Direct Least Squares Fitting of Ellipses," in *Proc. Int. Conf. Pattern Recognition*, 1996.

[8] A. W. Fitzgibbon, M. Pilu, and R. B. Fisher, "Direct Least Square Fitting of Ellipses," *IEEE Transactions on Pattern Analysis and Machine Intelligence*, **21**(5), pp. 476-480, 1999.

[9] J. D. Frost and J. S. Lai, "Digital Analysis of Aggregate Particle Shape," *Center For Aggregates Research Fourth Annual Symposium Proceedings*, 1996.

[10] W. Gander, G. H. Golub, and R. Strebel, "Least Squares Fitting of Circles and Ellipses," *BIT*, **34**(4) pp. 558-578, 1994.

[11] V. Gor, R. Castano, R. Manduchi, R. Anderson, and E. Mjolsness, "Autonomous Rock Detection For Mars Terrain," *American Institute of Aeronautics and Astronautics*, 2001.

[12] D. P. Huttenlocher, G. A. Klanderman, and W. J. Rucklidge, "Comparing Images Using the Hausdorff Distance," *IEEE Transactions on Pattern Analysis and Machine Intelligence*, **15**(9), pp. 850-863, 1993.

[13] J. Iivarinen, M. Peura, J. Sarela, and A. Visa, "Comparison of Combined Shape Descriptors For Irregular Objects," in *British Machine Vision Conference*, 1997.

[14] Y. Kanazawa and K. Kanatani, "Reliability of Fitting a Plane to Range Data," *IEICE Transactions on Information and Systems*, **E78-D-12**, pp. 1630-1635, 1995.

[15] W. C. Krumbein and L. L. Sloss, *Statigraphy and Sedimentation*, 1951.

[16] I. Kompatsiaris and M. G. Strintzis, "Spatiotemporal Segmentation and Tracking of Objects for Visualization of VideoConference Image Sequences," *IEEE Transactions on Circuits and Systems for Video Technology*, **10**(8), pp. 1388-1402, 2000.

[17] O. K. Kwon, D. G. Sim, and R. H. Park, "Hierarchical Hausdorff Distance Matching Algorithm Using Pyramidal Structures," *Proceedings of 4th Japan-Korea Joint Workshop on Computer Vision*, pp. 80-84, 1998.

[18] N. H. Maerz and W. Zhou, "Flat and Elongated: Advances Using Digital Image Analysis," *Center For Aggregates Research Seventh Annual Symposium Proceedings*, Austin, Texas, pp. BI-4-1 to BI-4-12.

[19] W. H. Press, S. A. Teukolsky, W. T. Vetterling, and B. P. Flannery, *Numerical Recipes in C*, pp. 394-455, 1997.

[20] D. F. Rogers and J. A. Adams, *Mathematical Elements for Computer Graphics*, Chpt. 4-6, 1990.

[21] P. L. Rosin, "A Note on the Least Squares Fitting of Ellipses," *Pattern Recognition Letters*, **14**, pp. 799-808, Oct. 1993.

[22] D.A. Turner, I. J. Anderson, J. C. Mason, and M. G. Cox, "An Algorithm for fitting an ellipsoid to data," Technical Report RR9803, School of Computing and Mathematics, University of Huddersfield, 1999.

[23] G. A. Watson, "Least squares fitting of parametric surfaces to measured data," *ANZIAM*, **42**(E), pp. C68-C95, 2000.

Justin Fox *is a Junior undergraduate at the California Institute of Technology majoring in Aerospace Engineering and Computer Science. He has spent two summer internships conducting research with the Machine Learning Systems Group at JPL. He plans on a career which would allow him to play a role in the exploration and development of space.*

Rebecca Castano *is a Senior Member of the Machine Learning Systems Group at the Jet Propulsion Laboratory. She received her Ph.D. in Electrical Engineering from the University of Illinois with her dissertion in the area of computer vision. Her research interests include machine learning, computer vision and pattern recognition.*

Robert C. Anderson *is a geologist at the Jet Propulsion Laboratory. Dr. Anderson was born in Anchorage, Alaska and raised in Newport News, Virginia. He attended Old Dominion University in Norfolk, Virginia, where he received his Bachelor of Science degree in geology in 1979. In 1985, he received a Master of Science from Old Dominion Unverisity in geology with an emphasis on structural geology and mapping tectonic features surrounding the Tharsis region of Mars. In 1995, he received a Doctor of Philosophy from the University of Pittsburgh in geology with an emphasis on visible and near infra-red remote sensing. His Ph.D. research was centering on mapping Quaternary surfaces and soils around the Whipple Mountains of southwestern Arizona.*

His current science research is centered on unraveling the geologic history of Mars with emphasis on understanding the tectonic and structural evolution of the Tharsis region. His recent publications in the Journal of Geophysical Research focused on identifying centers of tectonic activity with emphasis on identifying associated recent hydrothermal activity.

He is a Senior member of the Technical Staff at JPL and currently is employed as the Investigation Scientist for the Rock Abrasion Tool (RAT) and science support for mission operations on the Mars '03 mission.